Stress concentration of a micro-void embedded in a bi-layered material considering the boundary effects

Chunlin Wu, Ph.D.[1], Liangliang Zhang*, Ph.D.[2], and Huiming Yin, Ph.D.[3]

[1] Department of Civil Engineering and Engineering Mechanics,Columbia University,610 Seeley W. Mudd 500 West 120th St., New York, NY 10027.Email:cw3056@columbia.edu

[2]Department of Applied Mechanics, China Agricultural University, 301 Yifu Building 17 Qinghua East Road, Beijing, China 100083. Corresponding Author Email:llzhang@cau.edu.cn

[3] Department of Civil Engineering and Engineering Mechanics,Columbia University, 610 Seeley W. Mudd 500 West 120th St., New York, NY 10027. Email: yin@civil.columbia.edu

ABSTRACT

This paper extends the Eshelby's problem of one inhomogeneity embedded in a homogeneous infinite domain to a bi-material infinite domain. The equivalent inclusion method (EIM) is used to simulate the inhomogeneity by an inclusion with a polynomial eigenstrain. The fundamental solution of a point force in a bi-material is used to formulate the domain integral over the inclusion. For a finite bi-material domain, the boundary integral equation (BIE) takes into account the boundary responses by a single domain instead of utilizing the conventional multi-region BIE scheme. The EIM can similarly be used, and the elastic field can be obtained with tailorable accuracy based on the order of the polynomial eigenstrain. The algorithm is particularly suitable to simulate a defect in thin film/substrate systems or other similar bi-layered materials. Particularly, the stress concentration of a microvoid embedded in a bi-layered solar panel is investigated. The size and location of the void referred to the interface exhibits considerable effects on the stress concentration factor. Numerical case studies demonstrate the effectiveness and accuracy of the algorithm, and parametric studies show the boundary effects on the stress concentration of a microvoid in a finite bi-material under a uniform far field strain.

INTRODUCTION

The multi-layered systems have been widely utilized in versatile engineering and construction aspects, such as asphalt pavements (Yin and Prieto-Muñoz 2013), thin film surface coatings with protective and functional purposes (Abu-Thabit 2020; Ruys and Sutton 2021), and composite laminates (Anbusagar et al. 2015; Rana and Fangueiro 2016). However, the defects during manufacturing process, such as air voids, may significantly jeopardize the reliability and lifetime of the overall bi-material system. Sengab and Talreja (Sengab and Talreja 2016) summarized two main sources of those defects, (i) impurities and air evaporating during curing process; (ii) entrapment of air during manufacturing process. For example, in solar panel manufacturing (Yin et al. 2022b), any voids in a solar panel may disturb the light transmission, form hot spots under strong sunlight, and cause microcracks and failure of the solar panel. Even for a homogeneous encapsulate layer, the defects can cause stress concentrations leading to cracks and failure. Especially, when defects are close to the interface S, the discontinuity of stress across the interface augments the stress concentration and singularity effects. Therefore, high fidelity stress analysis may provide more insights to understand this phenomena.

To investigate the stress transfer between layered materials, Stoney (Stoney 1909) proposed an approach with plate system assumptions, such as thick substrate to ignore bending stiffness of thin film, equal twist curvatures and spatially constant surviving stress (Ngo et al. 2007). Because the strong assumptions violate practical applications, several subsequent extensions have been proposed to relax them (Wikström et al. 1999; Park and Suresh 2000). However, the Stoney theory ignores the shear stress transfer, modified theories (Haftbaradaran et al. 2012; Zhang et al. 2021) have been proposed to consider the interfacial sliding effects. Since the above previous works assume two dissimilar homogeneous material phases, therefore those models cannot provide accurate analysis for bi-material system with defects. Regarding influence brought by micro defects, Katnam et al. (Katnam et al. 2011) investigates the formulation of air voids with two adhesive mixing techniques and used X-ray to detect and evaluate porosity; Omairey et al. (Omairey et al. 2021) summarized several failure modes of adhesive joints of composites, where adhesive defects and substrate defects can cause high stress concentration leading to failures; Mishnaevsky (Mishnaevsky 2022) reported that even the defects in adhesive of the wind turbine blade may not dramatically disturb overall stress field, the local high stress concentration will lead to crack initiation.

To understand the effects of defects, the equivalent inclusion method (EIM) (Eshelby 1957; Eshelby 1959) was proposed to replace the defects with same matrix material along with inelastic strain, eigenstrain, to be determined by equivalent stress equations. With solved eigenstrain, the elastic fields can be acquired through superposition of initial fields and disturbance of eigenstrain, which is domain integral of fundamental solution over the inhomogeneity. Thanks to the versatility of fundamental solutions, EIM has been widely extended to other problems, such as heat conduction (Hatta and Taya 1986; Wu et al. 2021), dynamic elasticity (Song and Yin 2018), etc. The Eshelby's solution of one inhomogeneity over the infinite matrix ignores the interactions among inhomogeneities themselves and the boundary (Liu and Yin 2014; Wu and Yin 2021). Based on EIM, pioneers developed micromechanical models, such as the dilute, Mori-Tanaka(Mori and Tanaka 1973; Kanit et al. 2003; Yin and Zhao 2016) and self-consistent models (Hershey 1954; Kroner 1958), which provides effective mechanical properties of composites and bridge the microstructure and macroscopic behaviors. Other contributions on the homogenization schemes from linear elasticity to nonlinear rate-dependent problems can be found in (Zaoui 2002).

In the literature, several previous works explore the stress intensity factors (SIFs) caused by cracks and interfacial defects. Rather than using the conventional FEM, Treifi and Oyadiji (Treifi and Oyadiji 2013) proposed a fractal-like FEM to investigate SIFs of notch bodies with displacement interpolation functions. Bouhala et al. (Bouhala et al. 2013) developed crack-tip enrichment functions with extended FEM (XFEM) to study SIFs for cracks terminating at interface of bi-material; Pathak et al. (Pathak et al. 2011) combined element free Garlerkin method and XFEM on crack interaction problems. Kaddouri et al. (Kaddouri et al. 2006) studied a practical case with couple metal-ceramic on factors associated with perpendicular cracks to bi-material interface, such as distance of crack-tip to the interface.

As for boundary element method (BEM) with Kelvin's solution, the multi-region scheme is commonly used that interface of inhomogeneity and interface of bi-material require surface mesh and continuity equations are built to formulate the boundary value problem (BVP) (Beer et al. 2008; Liu et al. 2011). Fortunately, the continuity equations on interfaces of bi-material or multi-layered material can be mathematically considered with the fundamental solutions. Walpole (Walpole 1996) derived fundamental solutions to two-jointed dissimilar isotropic half-spaces through method of images; Yue (Yue 1995) proposed Yue's treatment, which is a generalized Kelvin's solution to multi-layered material; and other contributions in the literature can be found in review (Liu et al. 2011). Xiao et al. (Xiao et al. 2019) applied Yue's treatment (Yue 2015) in BEM to investigate semi-infinite transversely isotropic domain, especially for simulation of rocks. For a bi-material system, Yue's treatment can be reduced to explicit formulae, and Wu et al. (Wu et al. 2022) completed Walpole's solution and applied it for analysis of bi-material system. The above works, though, save efforts in discretizing bi-material interface, when the number of inhomogeneity increases, dimension scale varies or close to boundary, the multi-region scheme on inhomogeneity requires both considerable computational resources and preparation process.

In our recent work (Yin et al. 2022a), the algorithm of inclusion-based boundary element method (iBEM) is designed to handle drastically increase of DOFs in simulation of composites. Using technique of fundamental solution, the material mismatch between inhomogeneity and matrix can be simulated with eigenstrain field without mesh of subdomains. Compared with Eshelby's uniform eigenstrain assumption in (Eshelby 1957), eigenstrain is presented by Taylor series expansion at the centroid of inhomogeneity (Mura 1987). The algorithm iBEM combines the BEM and EIM, where the boundary effects and interactions between inhomogeneities are considered in BEM global matrix and equivalent stress equations, respectively. Solving the system of linear equations, the boundary responses and eigenstrain field can be obtained. The advantages of iBEM are: (i) for each inhomogeneity, the number of DOFs is fixed, 6, 24, 60 for uniform, linear and quadratic order, respectively; (ii) avoid any subdomain mesh, including bi-material interface and inhomogeneity and potential numerical errors brought by them; (iii) the merit of BEM and fundamental solution is retained that internal fields are expressed in boundary and domain integrals.

This paper aims to perform elastic analysis of an inhomogeneity embedded a bi-material system through the single-domain iBEM implemented with bi-material fundamental solution. In the following, the problem of a bi-material system with an inhomogeneity is firstly proposed, and then the fundamental solutions of bi-material, domain integrals over spherical inhomogeneity and global matrix of iBEM are introduced. Subsequently, the aforementioned iBEM is verified with FEM for a benchmark comparison. Applying the solution to a solar module containing a glass layer over a concrete panel, when a microvoild is embedded in the substrate, the SIFs are investigated with various distance to the bi-material interface. Finally, some conclusive remarks are discussed.

PROBLEM STATEMENT

Consider a domain $\mathcal{D}$ embedded with one subdomain Ω_1 is composed of two dissimilar isotropic domain, where the upper phase $\mathcal{D}^+$ and the lower phase $\mathcal{D}^-$ generally exhibits different material properties C' and C'', respectively. For instance, the stiffness tensor of $\mathcal{D}^+$ is $C'_{ijmn} = \lambda'\delta_{ij}\delta_{mn} + \mu'(\delta_{im}\delta_{jn} + \delta_{in}\delta_{jm})$, where λ' and μ' are lame constants of $\mathcal{D}^+$. The dimensions of the bi-material system are defined in Fig.1 that, (i) T_1 and T_2 are thickness of $\mathcal{D}^+$ and $\mathcal{D}^-$, respectively; (ii) l and b are length and width. Shown in Fig. 1, $\mathcal{D}$ is subjected to prescribed boundary conditions, where t_i and u_i represents surface traction and displacement, respectively. Without the loss of any generality, the bi-material interface S is chosen as parallel to plane $x_1 - x_2$ at $x_3 = 0$. In the following, two assumptions are made: (i) the embedded subdomain is filled with an isotropic material and its stiffness tensor C^I_{ijmn}; (ii) the bi-material and subdomain interfaces are perfect without any debonding behavior, which satisfy the continuity equations on both displacement and normal traction shown in Eq. (1).

$$u_i(\mathbf{x}^+) = u_i(\mathbf{x}^-), \quad \sigma_{ij}(\mathbf{x}^+)n_j(\mathbf{x}^+) = \sigma_{ij}(\mathbf{x}^-)n_j(\mathbf{x}^-) \tag{1}$$

where "+" and "-" represents the inward and outward side of the bi-material interface S or subdomain interface, respectively; $\mathbf{n}$ is the unit surface normal vector. Subsequently, the BVP can be formulated and it can be solved through the conventional multi-region scheme with interface mesh, which commonly demands high computational costs due to the singularity and discontinuity along the interface. This paper proposes an alternative method in which the fundamental solution for a bi-material infinite domain is directly applied to Eshelby's equivalent inclusion method and boundary integral method.

FORMULATION

Fundamental Solutions

Considering a two-jointed dissimilar half-spaces, the displacements at field point $\mathbf{x}$ can be expressed through the superposition of Kelvin's solution and image terms (Walpole 1996). The Green's function define the displacement response of any field point $\mathbf{x}$ caused by unit excitation at source point $\mathbf{x}'$. Given a unit concentrated force $f_j(\mathbf{x}') = n_j\delta(\mathbf{x}')$ ($\delta(\mathbf{x}')$ is the Dirac delta function) in the direction $\mathbf{n}$, the displacement variation can be expressed as,

$$u_i(\mathbf{x}') = G_{ij}(\mathbf{x}, \mathbf{x}') f_j(\mathbf{x}') \tag{2}$$

Due to the position of image terms, the fundamental solution differs whether source point $\mathbf{x}'$ and field point $\mathbf{x}$ are in the same material phase.

$$G^y_{ij}(\mathbf{x}, \mathbf{x}') = \frac{1}{4\pi\mu^w} \begin{cases} (\delta_{ij}\phi - \frac{\psi_{,ij}}{4(1-\nu^w)}) + A^y\overline{\phi}\delta_{ij} + \chi B^y(\delta_{i3}\delta_{jk} - \delta_{ik}\delta_{j3})\overline{\alpha}^y_{,k} \\ - C^y x_3\left[Q_J\overline{\psi}_{,ij3} + 4(1-\nu^w)\delta_{j3}\overline{\phi}_{,i} + 2(1-2\nu^w)\delta_{i3}Q_J\overline{\phi}_{,j} - Q_J x_3\overline{\phi}_{,ij}\right] & x'_3 x_3 \geq 0 \\ - D^y Q_I Q_J \overline{\psi}_{,ji} - (G^y + B^y) Q_J \overline{\beta}^y_{,ij} \\ \\ (\delta_{ij}\phi - \frac{\psi_{,ij}}{4(1-\nu^w)}) + A^y\phi\delta_{ij} + \chi B^y(\delta_{i3}\delta_{jk} - \delta_{ik}\delta_{j3})\alpha^y_{,k} & x'_3 x_3 < 0 \\ - D^y\psi_{,ij} - \chi x_3 F^y \alpha^y_{,ij} - (G^y + B^y) Q_I \beta^y_{,ji} \end{cases} \tag{3}$$

where the coeffcient $\chi = 1$, and superscripts $w =\,'$ and $y = u$ when $x'_3 \geq 0$; and $\chi = -1$, $w =\,''$ and $y = l$ when $x'_3 < 0$; $\mathbf{Q} = (1, 1, -1)$ is created for image terms through the interface S and the dummy index rule does not apply to capitalized ones; $\psi = |\mathbf{x} - \mathbf{x}'|$ is the Garlerkin distance vector and $\phi = \psi^{-1}$; $\frac{\delta_{ij}\phi}{4\pi\mu^w} - \frac{\psi_{,ij}}{16\pi(1-\nu^w)}$ is the Kelvin's solution of infinite space; $\overline{(.)}$ stands for image source points, such that $\overline{\psi} = |\mathbf{x} - \overline{\mathbf{x}'}|$ and $\overline{\mathbf{x}'} = (x_1', x_2', -x_3')$; $A^u - G^u$ are material constants related to the upper phase $\mathcal{D}^+$,

$$
\begin{aligned}
A^u = \frac{\mu' - \mu''}{\mu' + \mu''}, \quad B^u &= \frac{2\mu'(1-2\nu')(\mu'-\mu'')}{(\mu'+\mu'')(\mu'+\mu''(3-4\nu'))} \\
C^u = \frac{\mu' - \mu''}{2(1-\nu')(\mu' + (3-4\nu')\mu'')}, \quad D^u &= \frac{3-4\nu'}{2}C \\
F^u &= \frac{2\mu'(\mu'(1-2\nu'') - \mu''(1-2\nu'))}{(\mu'+\mu''(3-4\nu'))(\mu''+\mu'(3-4\nu''))} \\
G^u &= \frac{\mu'(\mu''(1-2\nu'')(3-4\nu') - \mu'(1-2\nu')(3-4\nu''))}{(\mu'+\mu''(3-4\nu'))(\mu''+\mu'(3-4\nu''))}
\end{aligned}
\tag{4}
$$

Similarly, coefficients $A^l - G^l$ can be obtained by switching two material phases, i.e. $A^l = \frac{\mu''-\mu'}{\mu''+\mu'}$. The other components in fundamental solution are listed below,

$$
\begin{aligned}
\alpha^u &= \ln[x_3' - x_3 + \psi], \quad \overline{\alpha}^u = \ln[x_3' + x_3 + \overline{\psi}] \\
\beta^u &= (x_3' - x_3)\alpha^u - \psi, \quad \overline{\beta}^u = (x_3' + x_3)\overline{\alpha}^u - \overline{\psi} \\
\alpha^l &= \ln[-x_3' + x_3 + \psi], \quad \overline{\alpha}^l = \ln[-x_3' - x_3 + \overline{\psi}] \\
\beta^l &= (-x_3' + x_3)\alpha^l - \psi, \quad \overline{\beta}^l = (-x_3' - x_3)\overline{\alpha}^l - \overline{\psi}
\end{aligned}
\tag{5}
$$

The α functions are also known as Bousinesq's displacement potentials, which are elaborated in Section "Domain Integral". According to Eqs.(2-4), when $C' = C''$, the coefficients $A - G$ vanishes and the fundamental solution reduce to Kelvin's solution; When one material phase exhibits zero stiffness, the fundamental solution reduces to the Mindlin's problem (Yin et al. 2022a).

One Inclusion in Two-jointed Dissimilar Half-spaces

Consider an infinite domain $\mathcal{D}$ composed of two-jointed dissimilar half-spaces, and one subdomain Ω_I is subjected to eigenstrain $\varepsilon_{ij}^*(\mathbf{x})$. Notice that although in Eshelby's work (Eshelby 1957; Eshelby 1959) the eigenstrain is constant over the subdomain, the eigenstrain indeed can vary spatially. Mura (Mura 1987) found that under interactions of inhomogeneities, the eigenstrain is not uniform anymore, and thus proposed to use the Taylor series expansion at the center of the subdomain to approximate eigenstrain as Eq.(6),

$$\varepsilon^*_{ij}(\mathbf{x}) = \varepsilon^{I0*}_{ij} + (x_p - x^{Ic}_p)\varepsilon^{I1*}_{ijp} + (x_p - x^{Ic}_p)(x_q - x^{Ic}_q)\varepsilon^{I2*}_{ijpq} \tag{6}$$

where $\mathbf{x}^{Ic}$ is centroid of Ω_I subdomain; $\varepsilon^{I0*}, \varepsilon^{I1*}$ and ε^{I2*} are uniform, linear and quadratic components of polynomial to approximate the eigenstrain. The disturbance displacement and strain field caused by eigenstrain can be obtained through the technique of Green's function as follows:

$$u_i(\mathbf{x}) = \int_{\Omega_I} \frac{\partial G_{ij}(\mathbf{x},\mathbf{x}')}{\partial x'_m}\varepsilon^*_{kl}(\mathbf{x}')C_{jmkl}(\mathbf{x}')\,dV(\mathbf{x}') = g_{ikl}\varepsilon^{I0*}_{kl} + g_{iklp}\varepsilon^{I1*}_{klp} + g_{iklpq}\varepsilon^{I2*}_{klpq} \tag{7}$$

$$\varepsilon_{ij}(\mathbf{x}) = S_{ijkl}\varepsilon^{I0*}_{kl} + S_{ijklp}\varepsilon^{I1*}_{klp} + S_{ijklpq}\varepsilon^{I2*}_{klpq} \tag{8}$$

where $g_{iklpq...} = \int_{\Omega_I} G_{ij,m'}C_{jmkl}(x'_p - x^{Ic}_p)(x'_q - x^{Ic}_q)\,dV(\mathbf{x}')$ is Eshelby's tensor for displacement; $S_{pq..ijkl} = \frac{g_{iklpq...,j}+g_{jklpq...,i}}{2}$ is Eshelby's tensor for strain; indices p,q mean that polynomial-form terms are involved, i.e $\psi_p = (x'_p - x^{Ic}_p)\psi$. Notice that comparing with Kelvin's solution, $G_{ij,m'} = -G_{ij,m}$ does not hold for bi-material fundamental solution and the partial derivatives are provided in Appendix I.

Domain Integrals of Fundamental Solution with Polynomial Terms

In Eq.(3), the fundamental solution is obtained through superposition of Kelvin's solution and image terms. As for Kelvin's solution, let Φ and Ψ denote domain integrals of ϕ and ψ, respectively. In 1891, Dyson (Dyson 1891) derived the general form domain integrals of elliptical shell with various density functions. Later Moschovidis and Mura (Moschovidis and Mura 1975) summarized Dyson's work and defined I and V functions to derive harmonic $\Phi_{pq...}$ and biharmonic $\Psi_{pq...}$ potentials, which will not be repeated below.

In terms of the image parts, let Θ and Λ denote the domain integrals of α and β, respectively. Walpole (Walpole 1997) firstly present Θ and Λ based on its definition of Bousinesq's displacement potential and Liu et al. (Liu et al. 2015) extended them up to quadratic order ($\Theta_{pq}, \Lambda_{pq}$). However, the authors only considered cases of $x_3' > 0$, thus in the following, we shall complete all cases of domain integrals with more simplified definitions.

In Eq.(5), four types of α and β functions are defined and the use of them is up to locations of source and field points. Following definition of displacement potentials, the functions can be rewritten as,

$$\begin{aligned} \alpha^u &= \int_{x_3}^{-\infty} \phi(x_1, x_2, t)\, dt \quad \overline{\alpha}^u = \int_{\infty}^{x_3} \overline{\phi}(x_1, x_2, t)\, dt \\ \alpha^l &= \int_{\infty}^{x_3} \phi(x_1, x_2, t)\, dt \quad \overline{\alpha}^l = \int_{x_3}^{-\infty} \overline{\phi}(x_1, x_2, t)\, dt \end{aligned} \tag{9}$$

where, only finite part of Eq.(9) are considered since infinite constant vanishes during partial differentiation. Similarly, β functions can be written as Eq.(9) with the same integral limits but switch integral functions from ϕ or $\overline{\phi}$ to α or $\overline{\alpha}$, respectively. Because both α and β functions are defined through integrals along the third axis with respect to field point, one can interchange the sequence of integral, taking Θ^u as an example,

$$\begin{aligned} \Theta^u &= \int_{\Omega_I} \alpha^u\, dV(\mathbf{x}') = \int_{x_3}^{-\infty} \int_{\Omega_I} \phi\, dV(\mathbf{x}')\, dt = \int_{x_3}^{-\infty} \Phi(x_1, x_2, t)\, dt \\ \Lambda^u &= \int_{\Omega_I} \beta^u\, dV(\mathbf{x}') = \int_{x_3}^{-\infty} \int_{\Omega_I} \alpha^u\, dV(\mathbf{x}')\, dt = \int_{x_3}^{-\infty} \Theta^u(x_1, x_2, t)\, dt \end{aligned} \tag{10}$$

Notice that for the integral with respect to t along the third axis does not include any integral points inside the subdomain, hence, only the exterior branch of Φ and Θ^u is retained. Following the same fashion, other Θ, Λ and their polynomial involved functions can be derived. In the following, their integrals are provided as below. The superscript s represents 4 types of functions defined in Eq.(9), which is up to locations of source and field points. $\phi^s = \overline{\phi}$, $\psi^s = \overline{\psi}$ when $x_3' x_3 \geq 0$ and $\phi^s = \phi$, $\psi^s = \psi$ when $x_3' x_3 < 0$

Uniform Domain Integrals Θ and Λ

$$\Theta^s = \frac{4\pi a^3}{3} \alpha^s \quad \& \quad \Lambda^s = \frac{4\pi a^3}{3} \beta^s \tag{11}$$

Linear Domain Integrals Θ_p and Λ_p

$$\Theta_p^s = \frac{4\pi a^5}{15}\begin{cases} -\alpha^s_{,p} & p \neq 3 \\ \phi^s & p = 3 \end{cases} \quad \& \quad \Lambda_p^s = \frac{4\pi a^5}{15}\begin{cases} -\beta^s_{,p} & p \neq 3 \\ \alpha^s & p = 3 \end{cases} \tag{12}$$

Quadratic Domain Integrals Θ_{pq} and Λ_{pq}

$$\Theta_{pq}^s = \frac{4\pi a^5}{105}\begin{cases} -a^2\alpha^s_{,q}(\alpha^s_{,p} + \ln[\psi^s]_{,p}) + \delta_{pq}[7\alpha^s + a^2\phi^s\gamma^s] & p, q \neq 3 \\ -a^2\phi^s_{,p} & p \neq 3, q = 3 \\ a^2\phi^s_{,3} + 7\alpha^s & p = q = 3 \end{cases} \tag{13}$$

and

$$\Lambda_{pq}^s = \frac{4\pi a^5}{105}\begin{cases} -a^2(x_p - x_p^{Ic})\gamma^s_{,q} + \delta_{pq}[7\beta^s - a^2\gamma^s] & p, q \neq 3 \\ -a^2\alpha^s_{,p} & p \neq 3, q = 3 \\ a^2\alpha^s_{,3} + 7\beta^s & p = q = 3 \end{cases} \tag{14}$$

where γ^s is argument of the logarithmic function (α^s). When $\alpha^s = \alpha^u$, we can obtain $\gamma^s = x_3' - x_3 + \psi$.

One Inhomogeneity in a Bounded Bi-material Domain

In the last subsection, the disturbance from polynomial-form eigenstrain can be obtained through the explicit domain integral of fundamental solution over the spherical subdomain Ω_I. Combining with the conventional BEM, the elastic field is superposition of boundary responses with BIEs and disturbance of eigenstrain with Eq.(7) and Eq.(8), and the displacement of arbitrary field point $\mathbf{x}$ within $\mathcal{D}^+$ can be expressed as,

$$\begin{aligned} u_i(\mathbf{x}) &= -\int_{\partial\mathcal{D}^t} T_{ij}(\mathbf{x}, \mathbf{x}')u_j(\mathbf{x}')d\mathbf{x}' + \int_{\partial\mathcal{D}^u} G_{ij}(\mathbf{x}, \mathbf{x}')t_j(\mathbf{x}')d\mathbf{x}' + \int_{\Omega_I} \frac{\partial G_{ij}(\mathbf{x}, \mathbf{x}')}{\partial x_m'}\varepsilon^*_{kl}(\mathbf{x}')C_{jmkl}(\mathbf{x}')\, dV(\mathbf{x}') \\ &= -\sum_{e=1}^{NE} H_{ij}u_j^e + \sum_{e=1}^{NE} U_{ij}t_j^e + g_{ikl}\varepsilon^{I0*}_{kl} + g_{iklp}\varepsilon^{I1*}_{klp} + g_{iklpq}\varepsilon^{I2*}_{klpq} \end{aligned} \tag{15}$$

where G_{ij} and $T_{ij} = \frac{C_{imkl}(\mathbf{x}')(G_{kj,l'}+G_{lj,k'})}{2} n_m(\mathbf{x}')$ are fundamental solution to displacement and traction, respectively. With boundary surface mesh, the BIEs are expressed in a discretization form (Beer et al. 2008) that $H_{ij} = \int_{S_e} T_{mi}(\mathbf{x},\mathbf{x}')N_{mj}(\mathbf{x}')\,dS$ and $U_{ij} = \int_{S_e} U_{mi}(\mathbf{x},\mathbf{x}')N_{mj}(\mathbf{x}')\,dS$; NE is the number of elements; the superscript e represents nodal values of boundary displacements and surface tractions in the e^{th} element. In Eq.(15), the interactions between subdomains and boundary are involved to displacement of BEM. Since the continuity conditions of bi-material interface S has been analytically considered in the fundamental solutions, one can solve the boundary response similar to a homogeneous matrix.

Unlike inclusion problems with prescribed eigenstrain, when the Ω^I is filled with different material C^I, the eigenstrain is yet to be determined with equivalent stress conditions. Mura (Mura 1987) proposed the conditions for polynomial-form eigenstrain to simulate material mismatch,

$$
\begin{aligned}
C^w_{ijkl}(\varepsilon^b_{kl} + \varepsilon'_{kl} - \varepsilon^{I0*}_{kl}) &= C^I_{ijkl}(\varepsilon^b_{kl} + \varepsilon'_{kl}) \\
C^w_{ijkl}(\varepsilon^b_{kl,m} + \varepsilon'_{kl,m} - \varepsilon^{I1*}_{klm}) &= C^I_{ijkl}(\varepsilon^b_{kl,m} + \varepsilon'_{kl,m}) \\
\frac{1}{2!}C^w_{ijkl}(\varepsilon^b_{kl,mn} + \varepsilon'_{kl,mn} - 2\varepsilon^{I2*}_{klmn}) &= \frac{1}{2!}C^I_{ijkl}(\varepsilon^b_{kl,mn} + \varepsilon'_{kl,mn})
\end{aligned}
\tag{16}
$$

Because the inhomogeneity may be located in either the upper phase $\mathcal{D}^+$ or the lower phase $\mathcal{D}^-$, in Eq.(16), the superscript $w ='$ when Ω^I is located is located in $\mathcal{D}^+$ and $w =''$ when Ω^I is located is located in $\mathcal{D}^-$. ε^b_{ij} is strain contributed by BIEs of boundary response with Eq.(20) in Appendix I; ε'_{ij} is disturbed strain field expressed in Eq.(8). As indicated in Eq.(16), the interaction of inhomogeneities are taken into account in equivalent stress conditions that one inhomogeneity can disturb stress field of another inhomogeneity. Therefore, assembling the conventional BEM matrix, collecting eigenstrain effects on boundary nodes and the stress equivalent equations, the iBEM global system of linear equations will be shown in Eq. (19) of Appendix I.

Discussion and extension to ellipsoidal inhomogeneity

In this article, the above single-domain iBEM algorithm aims to save efforts in handling of trivial procedures for domain discretization of the inhomogeneities. As for the industrial applications, Koenigsberger et al. (Königsberger et al. 2020) proposed a novel scheme on combination of Dvorak's transformation field analysis and Eshelby's method to investigate poro-elastic properties of cement paste, where the ellipsoidal Eshelby's tensor is introduced relating eigenstresses. In (Buchner et al. 2021) demonstrated experimental investigation on the effective elastic and thermal properties of clay bricks and various shapes of defects, i.e mesopores, quartz, are considered. Since the algorithm is based on the bi-material Green's function, and particularly the polynomial-form Eshelby's tensor used in equivalent stress conditions. Therefore, the limitations of the algorithm is the same limitation in the domain integral of the Green's function. Shown in Section "Domain integrals of fundamental solution with polynomial terms", the components of spherical Eshelby's tensor are derived by interchanging the integral sequence. Following the same fashion, (i) the domain integrals Φ and Ψ over an ellipsoidal region can be found in (Dyson 1891) and (Moschovidis and Mura 1975); (ii) the domain integrals Θ and Λ can be derived by partial integration along the third axis given integral limits. Notice that although Mura (Mura 1987) proposed the Taylor series expansion of eigenstrain to handle interactions of ellipsoidal inhomogeneities, when the ratios of axes of ellipsoid become too large / small, even quadratic eigenstrain terms may not provide accurate solution due to large variations of eigenstrain.

NUMERICAL VERIFICATION

The aforementioned algorithm is implemented to software package of iBEM to predict local fields of composites with prescribed boundary conditions. In order to validate the algorithm and illustrate how solutions with 3 orders of polynomial eigenstrain performs, a numerical case study with Robin's boundary condition is set up. Eshelby's solution of an inhomogeneity embedded in infinite space provides insight of uniform eigenstrain distribution. Actually, for a two-jointed half-spaces, if the inhomogeneity is far from the bi-material interface S, the image terms in fundamental solution Eq.(3) and its domain integral vanishes rapidly, which provides minor effects on stress disturbance. As a consequence, the elastic fields become similar to Eshelby's solution of infinite space. Therefore, the inhomogeneity will be placed close to the interface S to observe interfacial effects on elastic fields. For spherical inhomogeneities, the intensity of interaction is commonly judged by the ratio $d = h/a$, where a is radius and h is distance from the centroid to interface. Following the definition of Fig.1, the dimensions and boundary conditions are set as: (i) the width b, length l and two thickness T_1, T_2 are set as 1 m; (ii) the inhomogeneity with radius $a = 0.1$ m is placed in $\mathcal{D}^-$, where the distances h to interface S are $h = 1.1a, 2a$ and $3a$; (iii) shown in Fig.2, the top surface of $\mathcal{D}^+$ is subjected uniform downward pressure 1 MPa; and the displacement of bottom surface of $\mathcal{D}^-$ is constrained; all other four surfaces are free of traction. The shear modulus and Poisson's ratio for two material are $\mu' = 0.4$ MPa, $\nu' = 0.25$ and $\mu'' = 0.8$ MPa and $\nu'' = 0.1$, respectively.

Shown in Fig.3(a) and Fig.3(b), the elastic fields u_3 and σ_{33} are compared with FEM with different ratio of distance. Because the disturbance by the inhomogeneity vanishes rapidly, the $[-3, 3]a$ around the inhomogeneity is considered. In simulation, 1000 quadrilateral boundary elements are used in iBEM and $2, 189, 461$ tetrahedral elements are used in FEM. Regarding u_3, the curves agree well with FEM except minor discrepancy is observed in the second branch of case $h/a = 1.1$. In terms of stress comparison, the main discrepancy between iBEM and FEM exists at the interface between inhomogeneity Ω_I and matrix, which can be interpreted as intensive interfacial effects. Indicated in Fig.3(c), the stress concentration factors are compared in the vertical hoop of sphere and the maximum $\sigma_{\theta\theta}$ changes with intensivity of interfacial effects, specifically, in the case $h/a = 1.1$, the angle shifts near 14 degree. As the h/a increases, both stress concentration and angle shift decreases, which will be elaborated in "Ratio of Distance". In Fig.3(d), the stress σ_{33} $(h/a = 1.2)$ is compared along the center line among uniform, linear and quadratic series expansion. It is observed that the assumption of uniform distribution (Eshelby's solution) cannot predict the variation of elastic fields. The linear terms improves the accuracy but exhibit obvious discrepancy in the neighborhood of the inhomogeneity. Therefore, the introduction to quadratic term is necessary in improvement of accuracy of solution. In the comparison among uniform, linear and quadratic order terms, as shown in Fig. 3(d), the accuracy of predictions improves with the increase of polynomial order. Such phenomenon indicates that due to the existence of interfacial effects, none of the numerical solution (uniform, linear and quadratic) is exact solution and so does the FEM. Back to Fig. 3(c), except the curve $h/a = 1.1$, the other two cases $h/a = 2$ and $h/a = 3$ agree well with FEM. When the interfacial effects dominate, much more disturbance is observed, therefore, the disturbance also make the eigenstrain field more complex, which is the reason why even quadratic eigenstrains cannot provide adequately accuracy as iBEM exhibits an angle lag. When the distance ratio h/a increases and interfacial effects decrease accordingly, the uniform term gradually dominates the solution. In such case, only uniform term alone can provide accurate results (Wu and Yin 2021). Although the iBEM algorithm has enabled three tailorable accuracy options, in the following, quadratic term is applied to ensure reliable and accurate analysis.

CASE STUDY OF STRESS CONCENTRATION FACTORS

In the previous section, the iBEM algorithm has been validated with FEM with three cases of different distance ratios in a bi-material system. In this section, the algorithm is further utilized to investigate elastic fields and stress concentration factors of a specific industrial application with a microvoid $a = 2.5 \times 10^{-6}$m in the sunslate. Because of the thin adhesive layer, the sunslate can be considered as a bi-material system with $l = b = 0.1$ m of (i) glass ($E' = 72$GPa, $\nu' = 0.2, T_1$) and (ii) concrete panels ($E'' = 36$GPa, $\nu'' = 0.2, T_2$) (Yin et al. 2022b), as shown in Fig.1. The sunslate is subjected to downward pressure and thermal loads, which can be decomposed of superposition of free expansion and applied pressure for mismatch of thermal expansion coefficient (Yin and Prieto-Muñoz 2013), as shown in Fig.2. Since the free expansion does not result in variation of stress, this paper focus the second parts and the applied loads are set as 1MPa, which can be easily extended for other values of loads in linear elastic stage.

Ratio of Distance

The interfacial effects are judged through ratio of distance between the inhomogeneity and interface S. In this subsection, 8 ratio of distances are considered as $h/a = 1.1, 1.2, 1.4, 1.6, 1.8, 2, 2.5, 3$ and the microvoid is placed in lower and upper phase for overall 16 cases. In Fig.4(a) and Fig.4(b), the stresses $\sigma_{\theta\theta}$ are plotted versus the vertical hoop angle $\theta \in [-90°, 90°]$ when the microvoid is located in upper and lower phase, respectively. Comparing the angle of maximum stress, when

h/a increases and interfacial effects decrease, the angle gradually decreases accordingly. If h/a is large enough, the contribution from image terms in fundamental solutions vanishes and angle of maximum stress changes as zero, which is similar to a infinite space problem but with disturbed elastic fields due to the existence of the other phase. Obviously, the material mismatch influence the stress concentration as well. Indicated in Fig.4(a) and Fig.4(b), when microvoid is embedded in $\mathcal{D}^+$, the change of distance ratio exhibits larger variation of both angle shifts and stress concentration factor. In Fig.5(a), the angle shift in $\mathcal{D}^+$ is over 3 times than that of $\mathcal{D}^-$, which explains larger material mismatch amplify interfacial effects. Fig.4(c) shows the displacement u_3 of 6 cases of microvoid under uniform downward pressure 1 MPa on the vertical hoop. When the distance between microvoid and bottom surface decreases, the displacement u_3 decreases accordingly due to constraint of bottom surface. When angle $\theta = -90°$ and microvoid is embedded in $\mathcal{D}^+$, the differences between case “h/a = 1.1 - Upper" and “h/a = 1.2 - Upper" is larger than other angles. Such phenomenon is caused by interfacial effects associated with softer material concrete in $\mathcal{D}^-$. Similarly, when angle $\theta = 90°$ and microvoid is embedded in $\mathcal{D}^-$, opposite trend is observed. Shown in Fig.4(d), under horizontal pressure, the distance ratio has minor effects on stress concentration and angle shifts, which can be interpreted as the direction of load is perpendicular to x_3. Fig.5(b) exhibits the variation of stress concentration factor versus h/a with two types of loads and positions of microvoid. When h/a increases, the stress concentration factors tends to be constant, which is similar to Kelvin's problem.

Ratio of Shear Moduli

This subsection aims to present how ratio of shear moduli influence the stress concentration caused by the microvoid. Discussed in "Ratio of distance" section, besides the interfacial effects, the material mismatch also contribute to stress concentration. To avoid such factors, the microvoid is placed in the upper phase $\mathcal{D}^+$ with distance ratio $h/a = 1.2$ and the material properties of the upper phase remain the same ($E' = 72$GPa,$\nu' = 0.2$). 9 ratios of shear moduli $\frac{\mu'}{\mu''}$ are considered as 0.05, 0.1, 0.2, 0.5, 1, 2, 5, 10 and 20. Shown in Fig.6(a) and Fig.6(b), the stress concentration factors increases with μ'/μ'' and angle of maximum hoop stress shifts to negative range. When μ'/μ''

is small, the stiffer lower phase restrict the displacements and vice versa; consequently, as partial derivatives of displacements, the stress concentration factor is smaller and angle of maximum stress shifts to positive range. In Fig.6(c), when $\mu'/\mu'' = 1$, the fundamental solution reduces to Kelvin's solution, the stress concentration factor under vertical load is close to 2. Fig.6(d) plots the angle of maximum stress versus ratios of shear moduli and vertical load case has larger variations because the loading direction is perpendicular to the interface S. The angles of maximum stress in two curves are close to 5°, which is caused by non-uniformity of strain field around the microvoid (not a far-field uniform strain).

Ratio of Thickness

This subsection aims to investigate thickness ratio effects on the stress concentration behavior caused by the microvoid. Following the "Ratio of shear moduli", the microvoid is placed in $\mathcal{D}^+$ with distance ratio $h/a = 1.2$ and 6 ratios $1, 2, 5, 10, 15$ and 20 are selected. Fig.7(a) plots the vertical hoop stress with hoop angle. It is noticed that when $T_1/T_2 \leq 10$ and the ratio increases, the negative stress concentration factor decreases and positive stress concentration factor increases obviously. However, from case 15 and case 20, the trend reverses that case 20 has similar stress distribution as case 5; case 15 exists between case 10 and 5. Such phenomenon is caused by the elastic behavior of thin panels or plates. When the thickness ratio $T_1/T_2 \leq 10$, under horizontal pressure, the primary forces for $\mathcal{D}^+$ are bending and shear; as thickness ratio exceeds 10, the lateral shearing deformation become neglecting, which explains the maximum negative stress concentration increases due to elastic behavior change. Fig.7(b) indicates the trend of stress concentration factor discussed above. Under horizontal pressure, the horizontal hoop stress has similar trends as the other two curves. Notice that, unlike distance ratio and shear moduli ratio, the thickness ratio seldom change the angle of maximum negative/positive hoop stress. Because the angle shifts of maximum hoop stress is generally considered as interfacial effects, the smaller distance ratio, larger material mismatch and shear moduli ratio can augment such effects. However, the change of stress distribution with thickness ratios is mainly caused by the elastic behavior of the bi-material system itself.

CONCLUSIONS

The algorithm of the single domain inclusion-based boundary element method has been applied to investigate the elastic fields of bi-material system embedded with one microvoid. The algorithm has been verified by FEM with case study of void embedded in a two-cuboid bi-material system with different distance ratios. Along with the numerical verification, the iBEM with uniform, linear and quadratic terms are compared with FEM and provide tailorable accuracy upon readers' needs. Thanks to the fundamental solution of bi-material, and explicit domain integrals, the conventional boundary value problem with interface and subdomain can be solved similarly to a homogeneous solid. In this paper, the algorithm has been applied to study the stress concentration issues arisen in a Sunslate and parametric studies are conducted on effects brought by distance ratio, shear modulus ratio and thickness ratio and loading conditions. The algorithm is particularly suitable for understanding, designing and conducting virtual experiments on a thin-film system with potential defects.

Data Availability Statement

All data, models, or code that support the findings of this study are available from the corresponding author upon reasonable request.

Acknowledgments

This work is sponsored by the National Science Foundation IIP #1738802, IIP #1941244, CMMI#1762891, U.S. Department of Agriculture NIFA #2021-67021-34201, and National Natural Science Foundation of China (Grant No. 12102458), whose support is gratefully acknowledged.

APPENDIX I.

Method of images in Walpole's solution and its modified form

This appendix subsection aims to provide details and discussion of fundamental solution by Walpole (Walpole 1996). For a perfect bounded bi-material interface, the continuity conditions in Eq. (1) on displacements and tractions need to be satisfied. The method of images is a typical mathematical tool to solve partial differential equations that a mirror image source is artificially created to handle the continuity conditions of the interface without extending the domain of function. Haberman (Haberman 2021) illustrated the method through semi-infinite solution to Poisson's equation in Chapter 9.5.8 and transient heat transfer in Chapter 11.5.3. Walpole (Walpole 1996) wrote the fundamental solution (displacement) in terms of two branches, which are determined by positions of field and source points. Subsequently, similar to Boussinesq's solution and Mindlin's problem, the potential functions are assumed as partial integration with respect to the third axis, where part of Kelvin's solution and nuclei of strain are applied. According to the continuity conditions, the coefficients associated with material constants can be determined.

The original form of bi-material elastic fundamental solution can be applied to investigated induced elastic fields caused by loads at any arbitrary interior point. However, its application to Eshelby's problem is not complicated and trivial as Eshelby's tensor leads domain integrals with the free source terms, i.e x_3'. It is possible to represent the free source terms with Garlekin's distance vector, for example, the domain integral of $x_3'\phi$ can altered as $\int_\Omega (x_3' - x_3) + x_3\phi d\mathbf{x}' = -\Psi_{,3} + x_3\Phi$, which simplifies the domain integral expressions.

Partial Derivatives of Domain Integrals

It is noted that with image terms, partial differentiation process changes accordingly, say $\overline{\alpha}^u_{,i'} = -Q_I\overline{\alpha}^u$, we provide the first order derivative of fundamental solution to obtain Eshelby's tensor for displacement with quadratic order polynomial,

(1) When $x'_3 x_3 \geq 0$,

$$
\begin{aligned}
&4\pi\mu^w \int_\Omega (x'_p - x^c_p)(x'_q - x^c_q) G_{ij,m'}\, dV(\mathbf{x}') \\
&= (-\delta_{ij}\Phi_{pq,m} + \frac{\Psi_{pq,ijm}}{4(1-\nu^w)}) - Q_P Q_Q \Big\{ A^y \delta_{ij} Q_M \overline{\Phi}_{pq,m} - \chi B^y Q_M (\delta_{i3}\overline{\Theta}^y_{pq,jm} - \delta_{j3}\overline{\Theta}^y_{pq,im}) \\
&- C^y x_3 Q_M \Big[- Q_J \overline{\Psi}_{pq,ij3m} - 4(1-\nu^w)\delta_{j3}\overline{\Phi}_{pq,im} - 2(1-2\nu^w)\delta_{i3} Q_J \overline{\Phi}_{pq,jm} + x_3 Q_J \overline{\Phi}_{pq,ijm} \Big] \\
&+ Q_J Q_M \Big[D^c Q_I \overline{\Psi}_{pq,ijm} + (G^y + B^y)\overline{\Lambda}^y_{pq,ijm} \Big] \Big\}
\end{aligned}
\tag{17}
$$

(2) When $x'_3 x_3 < 0$,

$$
\begin{aligned}
&4\pi\mu^w \int_\Omega (x'_p - x^c_p)(x'_q - x^c_q) G_{ij,m'}\, dV(\mathbf{x}') \\
&= (-\delta_{ij}\Phi_{pq,m} + \frac{\Psi_{pq,ijm}}{4(1-\nu^w)}) - A^y \delta_{ij}\Phi_{pq,m} - \chi B^y (\delta_{i3}\Theta^y_{pq,jm} - \delta_{j3}\Theta^y_{pq,im}) \\
&+ D^y \Psi_{pq,ijm} + \chi x_3 F^y \Theta^c_{pq,ijm} + (G^y + B^y) Q_I \Lambda^y_{pq,ijm}
\end{aligned}
\tag{18}
$$

For other higher order derivatives to obtain Eshelby's tensor for strain is straightforward because the partial differentiation is with respect to x_n not x'_n.

Global Matrix of iBEM

$$
\begin{bmatrix}
\mathcal{H} + H & \dots & -g^{0I} & -g^{1I} & -g^{2I} & \dots \\
\vdots & \vdots & \vdots & \vdots & \vdots & \vdots \\
\Delta C^I H^{1I} & \dots & \Delta C^I S^{0I} & \Delta C^I S^{1I} & \Delta C^I S^{2I} & \dots \\
\Delta C^I H^{2I} & \dots & \Delta C^I S^{0I'} & \Delta C^I S^{1I'} & \Delta C^I S^{2I'} & \dots \\
\Delta C^I H^{3I} & \dots & \Delta C^I S^{0I''} & \Delta C^I S^{1I''} & \Delta C^I S^{2I''} & \dots \\
\vdots & \vdots & \vdots & \vdots & \vdots & \vdots
\end{bmatrix}_{(3*NN+s*NI)\times(3*NN+s*NI)}
\begin{bmatrix} u \\ \vdots \\ \varepsilon^{*0I} \\ \varepsilon^{*1I} \\ \varepsilon^{*2I} \\ \vdots \end{bmatrix}_{(3*NN+s*NI)}
=
\begin{bmatrix} U \\ \vdots \\ -\Delta C^I U^{1I} \\ -\Delta C^I U^{2I} \\ -\Delta C^I U^{3I} \\ \vdots \end{bmatrix}_{(3*NN+s*NI)\times(3*NN)}
\begin{bmatrix} t \end{bmatrix}_{(3*NN)}
\tag{19}
$$

where s is determined order of polynomial by users, as 6, 24, 60 for uniform, linear and quadratic; $\mathcal{H}$ is a diagonal matrix applied in conventional BEM to eliminate strong singularities with method of rigid body motion for static problems; H and U are coefficients calculated by discretized BIE in Eq.(15); g and S are Eshelby's tensor for displacement and strain (with uniform, linear and quadratic order), respectively; H^{1I}, H^{2I}, H^{3I} and U^{1I}, U^{2I}, U^{3I} are coefficients calculated by discretized BIE in Eq.(20) below for strain, first order partial derivative of strain and second order partial derivatives of strain, respectively. They are used in equivalent stress conditions as Eq.(16).

$$\begin{aligned} U^{0I}_{ijm} &= \frac{1}{2}\int_{S_e} (H_{ik,j}(\mathbf{x},\mathbf{x}') + H_{jk,i}(\mathbf{x},\mathbf{x}'))N_{mk}(\mathbf{x}')\, dS \\ H^{0I}_{ijm} &= \frac{1}{2}\int_{S_e} (T_{ik,j}(\mathbf{x},\mathbf{x}') + T_{jk,i}(\mathbf{x},\mathbf{x}'))N_{mk}(\mathbf{x}')\, dS \end{aligned} \tag{20}$$

Similarly, other higher order partial derivatives can be obtained, i.e, $U^{2I}_{ijmnr} = \frac{1}{2}\int_{S_e}(H_{ik,jnr}(\mathbf{x},\mathbf{x}') + H_{jk,inr}(\mathbf{x},\mathbf{x}'))N_{mk}(\mathbf{x}')\, dS$.

APPENDIX II. COMPUTATIONAL TESTS BETWEEN IBEM AND FEM

This appendix section aims to provide details in computational efficiency and accuracy comparison between the proposed iBEM programmed by authors and FEM using a commercial software ANSYS. Regarding the accuracy and convergence, two aspects are discussed, (a) a convergence analysis of FEM through refinement of elements around the inhomogeneity; and (b) an error analysis concerning the differences between iBEM and FEM (convergent results). As for the efficiency, three main aspects are considered, (i) preparation stage, such as generation of geometric specification ,surface (iBEM) / volume (FEM) domain discretization; (ii) construction and solving process, such as computation of global matrix and solution time; and (iii)a comparison occupancy test of CPU and RAM in two methods.

Without the loss of any generality, this section follows "Numerical Verification" that all material properties are retained and the ratio of distance $h/a = 1.5$, where the inhomogeneity with radius $a = 0.1$ m is located in the lower phase $\mathcal{D}^-$. For BEM surface mesh, 4-node bi-linear quadrilateral elements with 4 Gauss integral points are used with adaptive subdivision integration scheme following (Eberwien et al. 2005). Regarding FEM volume mesh, 10-node quadratic tetrahedral elements are used due to expected larger variation of displacements.

Accuracy test

Shown as Fig. 8, in order to use fewer elements, the neighbor box (dimension $0.4\times0.4\times0.3$ m) with the spherical inhomogeneity and the rest region of the matrix are treated with two mesh sizes. Four internal size steps are selected as 0.04, 0.015, 0.008 and 0.006 m, while the uniform external mesh size is 0.04 m. When the internal mesh size decreases, the number of elements increase accordingly as 41, 4906, 50, 9469, 114, 7928 and 232, 6729. Indicated in Fig. 9(a), the stress concentration factor $\sigma_{\theta\theta}/\sigma^0_{33}$ gradually converges as the differences between size steps decrease. Particularly, size step 0.006 and 0.008 exhibit very minor discrepancies, and the two curves also agree well with results in iBEM. Considering the larger differences in Fig. 3(c), when the distance ratio h/a increase, the variation in eigenstrain decreases accordingly, which can provide good predictions. Fig. 9(b) indicates the errors between iBEM and two FEM curves, although there are some differences, considering the maximum stress concentration factor is 1.94, the errors between two methods are acceptable.

Efficiency test

Shown as Table. 1, FEM and iBEM-quadratic used 2 and 8 cores, respectively. We keep the default setting of ANSYS, which limits participation of more cores, so that the solving time will be shorter. Since the solving process contains calculation, assignment of coefficients and matrix decomposition, the solution time is not linearly proportional to number of cores, because assignment of coefficients is partially a single-thread process. Although Table. 1 indicates iBEM package occupies all cores of the CPU, it uses “Eigen" library, where the process decomposition of matrix is not fully multi-core. The iBEM-quadratic exhibit apparent advantages on RAM usage over FEM, because the degree of freedom is a constant as $3,060$. Regarding the mesh process, iBEM only require the surface mesh, which avoids trivial process on the inhomogeneity and its neighbor region as shown in Fig. 8 (d). In addition, FEM require specification of models, such as importing from AutoCAD or creating in its own geometry editors, which requires more efforts. Considering all above factors, iBEM would be an efficient and computational resource friendly scheme.

REFERENCES

Abu-Thabit, N. Y. (2020). "Electrically conducting polyaniline smart coatings and thin films for industrial applications." *Advances in Smart Coatings and Thin Films for Future Industrial and Biomedical Engineering Applications*, Elsevier, 585–617.

Anbusagar, N., Palanikumar, K., and Giridharan, P. (2015). "Study of sandwich effect on nanoclay modified polyester resin GFR face sheet laminates." *Composite Structures*, 125, 336–342.

Beer, G., Smith, I., and Duenser, C. (2008). *The Boundary Element Method with Programming*. Springer Vienna.

Bouhala, L., Shao, Q., Koutsawa, Y., Younes, A., Núñez, P., Makradi, A., and Belouettar, S. (2013). "An XFEM crack-tip enrichment for a crack terminating at a bi-material interface." *Engineering Fracture Mechanics*, 102, 51–64.

Buchner, T., Kiefer, T., Königsberger, M., Jäger, A., and Füssl, J. (2021). "Continuum micromechanics model for fired clay bricks: Upscaling of experimentally identified microstructural features to macroscopic elastic stiffness and thermal conductivity." *Materials & Design*, 212, 110212.

Dyson, F. W. (1891). "The potentials of ellipsoids of variable densities." *The Quarterly Journal of Pure and Applied Mathematics*.

Eberwien, U., Duenser, C., and Moser, W. (2005). "Efficient calculation of internal results in 2d elasticity bem." *Engineering Analysis with Boundary Elements*, 29, 447–453.

Eshelby, J. D. (1957). "The determination of the elastic field of an ellipsoidal inclusion, and related problems." *Proceedings of the Royal Society of London. Series A. Mathematical and Physical Sciences*, 241(1226), 376–396.

Eshelby, J. D. (1959). "The elastic field outside an ellipsoidal inclusion." *Proceedings of the Royal Society of London. Series A. Mathematical and Physical Sciences*, 252(1271), 561–569.

Haberman, R. (2021). *Applied Partial Differential Equations with Fourier Series and Boundary Value Problems (Classic Version), 5th Edition*. Pearson.

Haftbaradaran, H., Soni, S. K., Sheldon, B. W., Xiao, X., and Gao, H. (2012). "Modified stoney equation for patterned thin film electrodes on substrates in the presence of interfacial sliding."

Journal of Applied Mechanics, 79(3).

Hatta, H. and Taya, M. (1986). "Thermal conductivity of coated filler composites." *Journal of Applied Physics*, 59(6), 1851–1860.

Hershey, A. V. (1954). "The elasticity of an isotropic aggregate of anisotropic cubic crystals." *Journal of Applied Mechanics*, 21(3), 236–240.

Kaddouri, K., Belhouari, M., Bouiadjra, B. B., and Serier, B. (2006). "Finite element analysis of crack perpendicular to bi-material interface: Case of couple ceramic–metal." *Computational Materials Science*, 35(1), 53–60.

Kanit, T., Forest, S., Galliet, I., Mounoury, V., and Jeulin, D. (2003). "Determination of the size of the representative volume element for random composites: statistical and numerical approach." *International Journal of Solids and Structures*, 40(13-14), 3647–3679.

Katnam, K., Stevenson, J., Stanley, W., Buggy, M., and Young, T. (2011). "Tensile strength of two-part epoxy paste adhesives: Influence of mixing technique and micro-void formation." *International Journal of Adhesion and Adhesives*, 31(7), 666–673.

Kroner, E. (1958). "Berechnung der elastischen konstanten des vielkristalls aus den konstanten des einkristalls." *Z. Physik*, 151(4), 504–518.

Königsberger, M., Pichler, B., and Hellmich, C. (2020). "Multiscale poro-elasticity of densifying calcium-silicate hydrates in cement paste: An experimentally validated continuum micromechanics approach." *International Journal of Engineering Science*, 147, 103196.

Liu, Y. J., Mukherjee, S., Nishimura, N., Schanz, M., Ye, W., Sutradhar, A., Pan, E., Dumont, N. A., Frangi, A., and Saez, A. (2011). "Recent advances and emerging applications of the boundary element method." *Applied Mechanics Reviews*, 64(3).

Liu, Y. J., Song, G., and Yin, H. M. (2015). "Boundary effect on the elastic field of a semi-infinite solid containing inhomogeneities." *Proceedings of the Royal Society A: Mathematical, Physical and Engineering Sciences*, 471(2179), 20150174.

Liu, Y. J. and Yin, H. M. (2014). "Stress concentration of a microvoid embedded in an adhesive layer during stress transfer." *Journal of Engineering Mechanics*, 140(10), 04014075.

Mishnaevsky, L. (2022). “Root causes and mechanisms of failure of wind turbine blades: Overview.” *Materials*, 15(9), 2959.

Mori, T. and Tanaka, K. (1973). “Average stress in matrix and average elastic energy of materials with misfitting inclusions.” *Acta Metallurgica*, 21(5), 571–574.

Moschovidis, Z. A. and Mura, T. (1975). “Two-ellipsoidal inhomogeneities by the equivalent inclusion method.” *Journal of Applied Mechanics*, 42(4), 847–852.

Mura, T. (1987). “Micromechanics of defects in solids (martinus nijhoff, dordrecht, 1987).” *and*, 179, 149.

Ngo, D., Feng, X., Huang, Y., Rosakis, A., and Brown, M. (2007). “Thin film/substrate systems featuring arbitrary film thickness and misfit strain distributions. part i: Analysis for obtaining film stress from non-local curvature information.” *International Journal of Solids and Structures*, 44(6), 1745–1754.

Omairey, S., Jayasree, N., and Kazilas, M. (2021). “Defects and uncertainties of adhesively bonded composite joints.” *SN Applied Sciences*, 3(9).

Park, T.-S. and Suresh, S. (2000). “Effects of line and passivation geometry on curvature evolution during processing and thermal cycling in copper interconnect lines.” *Acta Materialia*, 48(12), 3169–3175.

Pathak, H., Singh, A., and Singh, I. V. (2011). “Numerical simulation of bi-material interfacial cracks using EFGM and XFEM.” *International Journal of Mechanics and Materials in Design*, 8(1), 9–36.

S. Rana and R. Fangueiro, eds. (2016). *Advanced Composite Materials for Aerospace Engineering*. Elsevier.

Ruys, A. J. and Sutton, B. A. (2021). “Metal-ceramic functionally graded materials (FGMs).” *Metal-Reinforced Ceramics*, Elsevier, 327–359.

Sengab, A. and Talreja, R. (2016). “A numerical study of failure of an adhesive joint influenced by a void in the adhesive.” *Composite Structures*, 156, 165–170.

Song, G. and Yin, H. M. (2018). “Stress concentration of one microvoid embedded in an adhesive layer under harmonic load." *Journal of Engineering Mechanics*, 144(3), 04018002.

Stoney, G. G. (1909). "The tension of metallic films deposited by electrolysis." *Proceedings of the Royal Society of London. Series A, Containing Papers of a Mathematical and Physical Character*, 82(553), 172–175.

Treifi, M. and Oyadiji, S. O. (2013). "Evaluation of mode III stress intensity factors for bi-material notched bodies using the fractal-like finite element method." *Computers & Structures*, 129, 99–110.

Walpole, L. (1996). "An elastic singularity in joined half-spaces." *International Journal of Engineering Science*, 34(6), 629–638.

Walpole, L. (1997). "An inclusion in one of two joined isotropic elastic half-spaces." *IMA Journal of Applied Mathematics*, 59(2), 193–209.

Wikström, A., Gudmundson, P., and Suresh, S. (1999). "Thermoelastic analysis of periodic thin lines deposited on a substrate." *Journal of the Mechanics and Physics of Solids*, 47(5), 1113–1130.

Wu, C., Wei, Z., and Yin, H. (2021). "Virtual and physical experiments of encapsulated phase change material embedded in building envelopes." *International Journal of Heat and Mass Transfer*, 172, 121083.

Wu, C. and Yin, H. (2021). "The inclusion-based boundary element method (iBEM) for virtual experiments of elastic composites." *Engineering Analysis with Boundary Elements*, 124, 245–258.

Wu, C., Zhang, L., Cui, J., and Yin, H. (2022). "Three dimensional elastic analysis of a bi-material system with a single domain boundary element method (accepted)." *Engineering Analysis with Boundary Elements*.

Xiao, S., Yue, Z. Q., and Xiao, H. (2019). "Boundary element analysis of transversely isotropic bi-material halfspaces with inclined planes of isotropy and interfaces." *International Journal for Numerical and Analytical Methods in Geomechanics*, 43(17), 2599–2627.

Yin, H., Song, G., Zhang, L., and Wu, C. (2022a). *The Inclusion-Based Boundary Element Method* *(iBEM)*. Academic Press.

Yin, H., Zadshir, M., and Pao, F. (2022b). *Building Integrated Photovoltaic Thermal Systems*. Elsevier.

Yin, H. and Zhao, Y. (2016). *Introduction to the Micromechanics of Composite Materials*. CRC Press (jan).

Yin, H. M. and Prieto-Muñoz, P. A. (2013). "Stress transfer through fully bonded interface of layered materials." *Mechanics of Materials*, 62, 69–79.

Yue, Z. Q. (1995). "On generalized kelvin solutions in a multilayered elastic medium." *Journal of Elasticity*, 40(1), 1–43.

Yue, Z. Q. (2015). "Yue's solution of classical elasticity in n-layered solids: Part 1, mathematical formulation." *Frontiers of Structural and Civil Engineering*, 9(3), 215–249.

Zaoui, A. (2002). "Continuum micromechanics: Survey." *Journal of Engineering Mechanics*, 128(8), 808–816.

Zhang, Y., Lin, Q., and Yin, H. (2021). "Thermoelastic modeling of layered composites considering bending and shearing effects." *Journal of Engineering Mechanics*, 147(7), 04021034.

List of Tables

TABLE 1. Comparison of efficiency among iBEM with quadratic terms and FEM with four internal size steps

	CPU Usage (cores)	RAM Usage (Gb)	Mesh time (s)	Solving time (s)
FEM-0.04	2	2.22	17	48
FEM-0.015	2	3.51	27	58
FEM-0.008	2	7.65	39	133
FEM-0.006	2	12.60	72	326
iBEM-quadratic	8	0.58	5	10.2
CPU: i7-9700K (8 cores)	RAM: 2933mHz			

List of Figures

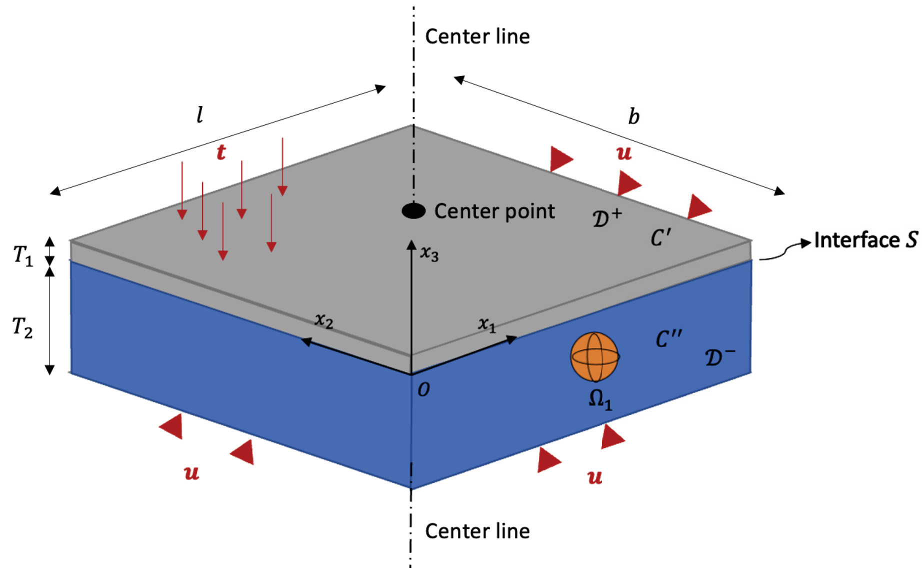

Fig. 1. Schematic plot of a bi-material system $\mathcal{D}$ (a) subjected to mixed prescribed boundary conditions embedded with one inhomogeneity Ω_I

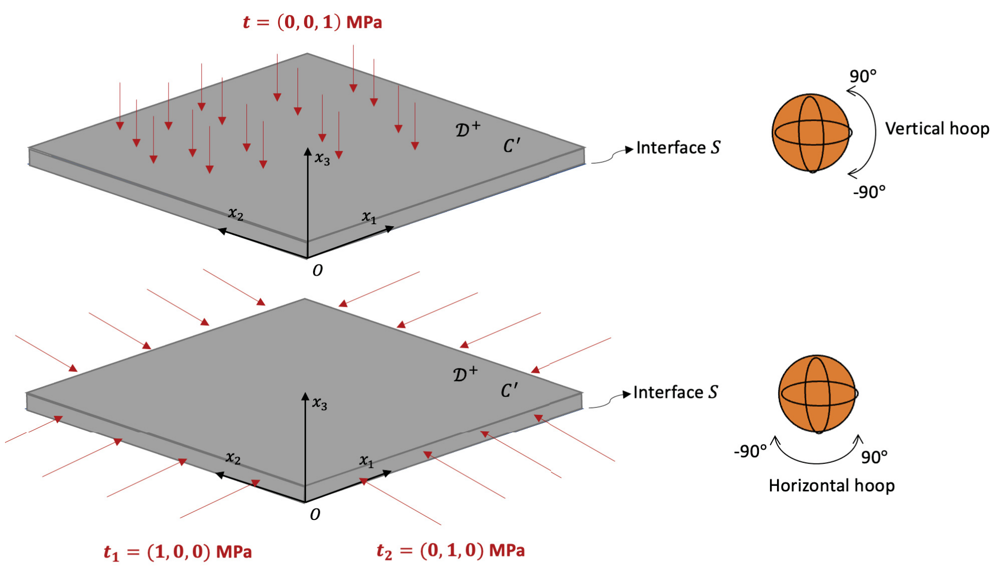

Fig. 2. Downward pressure and horizontal pressure loading cases and vertical/horizontal for stress comparison

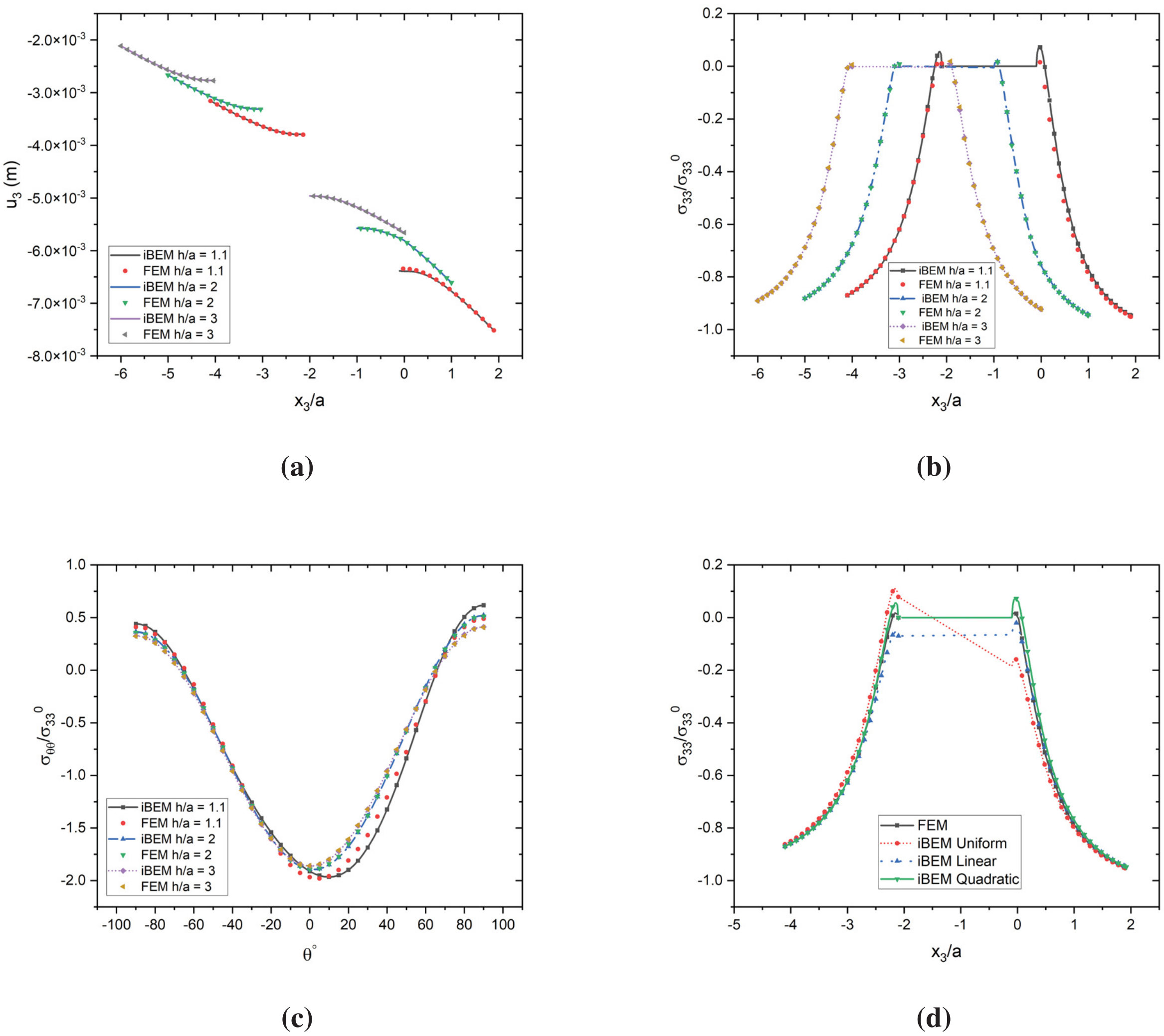

Fig. 3. Variation and comparison with FEM of elastic fields disturbed by void versus distance ratio h/a (a) u_3, (b) ratio of normal stress $\sigma_{33}/\sigma_{33}^0$ along the center line; (c) stress concentration factor along the vertical hoop $[-90, 90]^\circ$; (d) comparison of uniform, linear and quadratic polynomial eigenstrain expansion along the center line

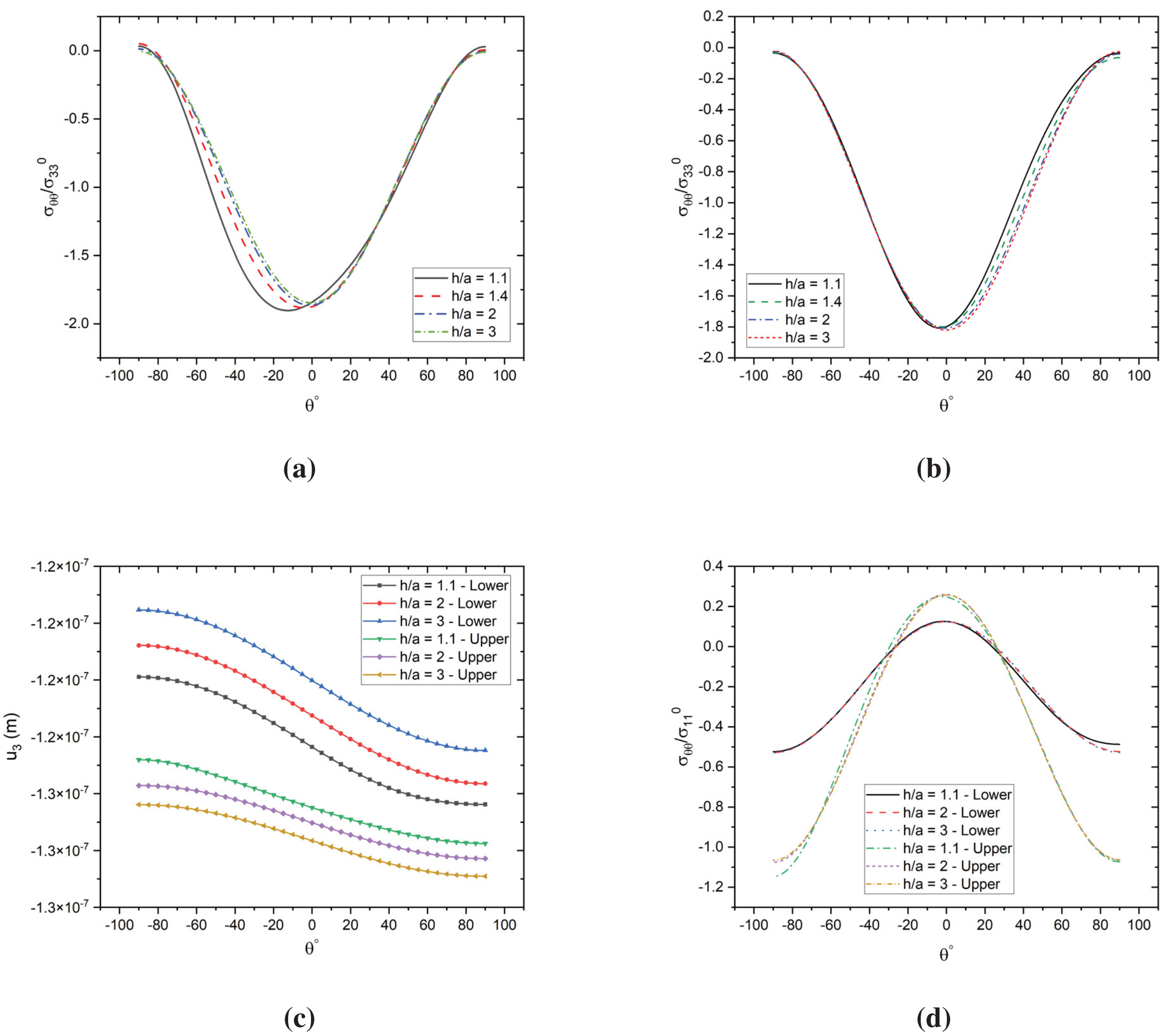

Fig. 4. Variation of elastic fields disturbed by the microvid versus 8 distance ratios, (a) vertical hoop stress $\sigma_{\theta\theta}$ and $\Omega_I \in \mathcal{D}^+$ (b) vertical hoop stress $\sigma_{\theta\theta}$ and $\Omega_I \in \mathcal{D}^-$ (c) displacement u_3 under uniform downward pressure 1 MPa; (d) vertical hoop stress $\sigma_{\theta\theta}$ under two horizontal pressure 1 MPa

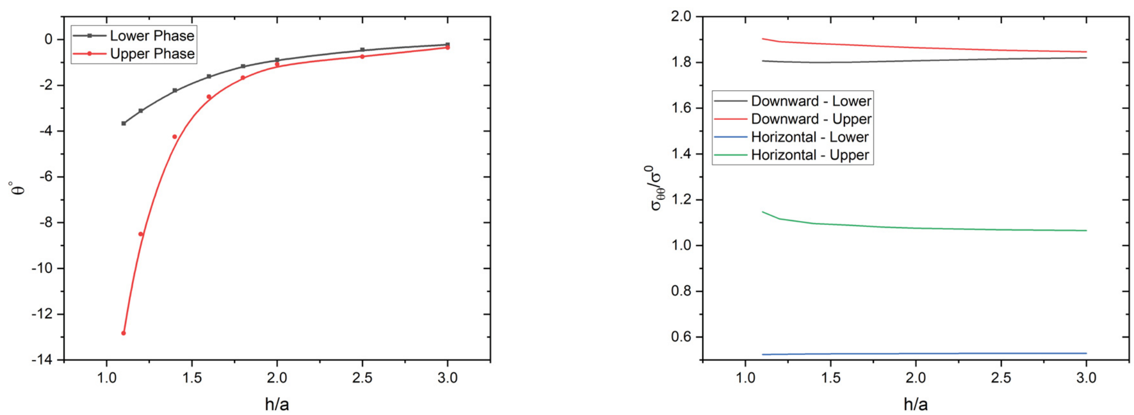

(a) **(b)**

Fig. 5. Variation of stress concentration versus 8 distance ratios, (a) angle shifts under uniform downward pressure 1MPa and (b) stress concentration factors under uniform downward / horizontal pressure 1MPa

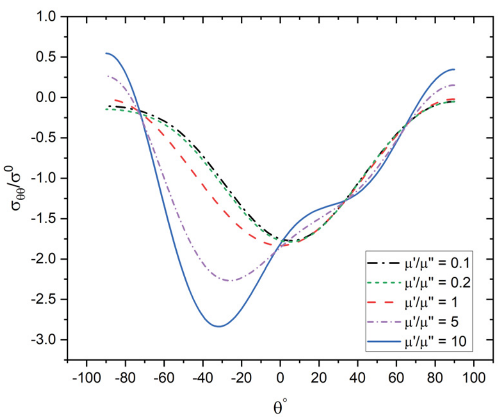

(a)

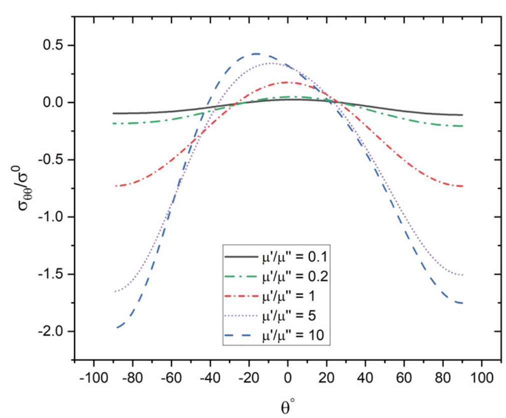

(b)

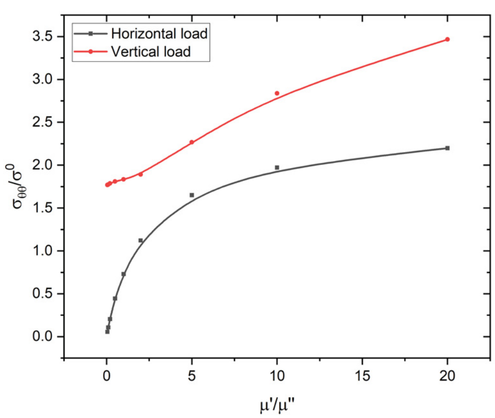

(c)

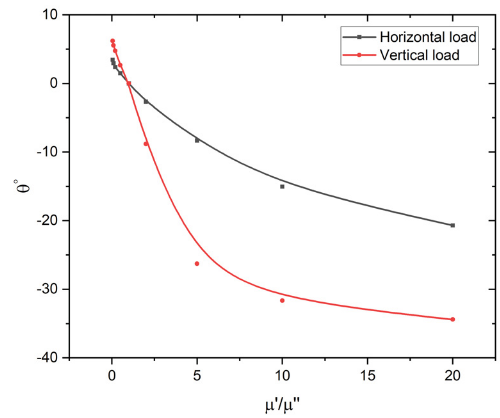

(d)

Fig. 6. Variation of elastic fields disturbed by microvoid versus ratios of shear moduli μ'/μ'', (a) vertical hoop stress $\sigma_{\theta\theta}$ under uniform downward pressure; (b) vertical hoop stress $\sigma_{\theta\theta}$ under horizontal pressure; (c) stress concentration factor;(d) angle shifts of maximum hoop stress of two loading cases

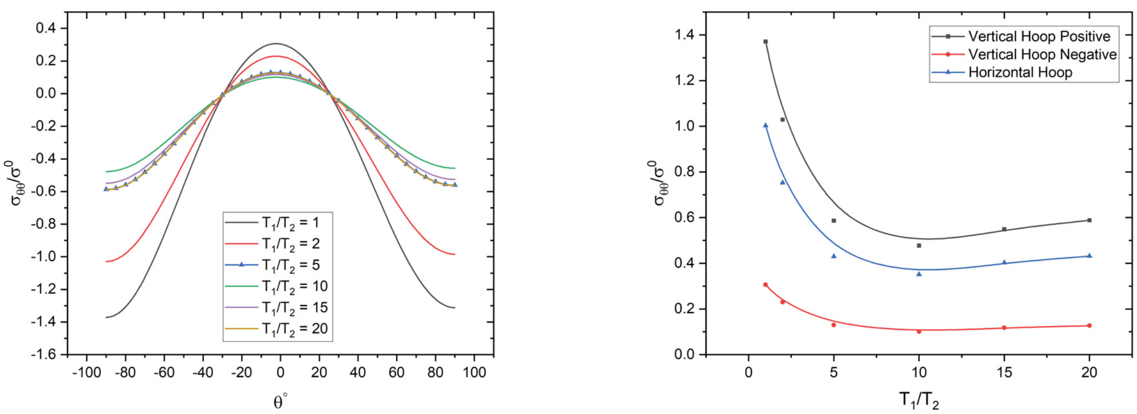

(a) **(b)**

Fig. 7. Variation of elastic fields disturbed by microvoid under horizontal pressure versus thickness ratio T_1/T_2, (a) vertical hoop stress $\sigma_{\theta\theta}$; (b) stress concentration factor

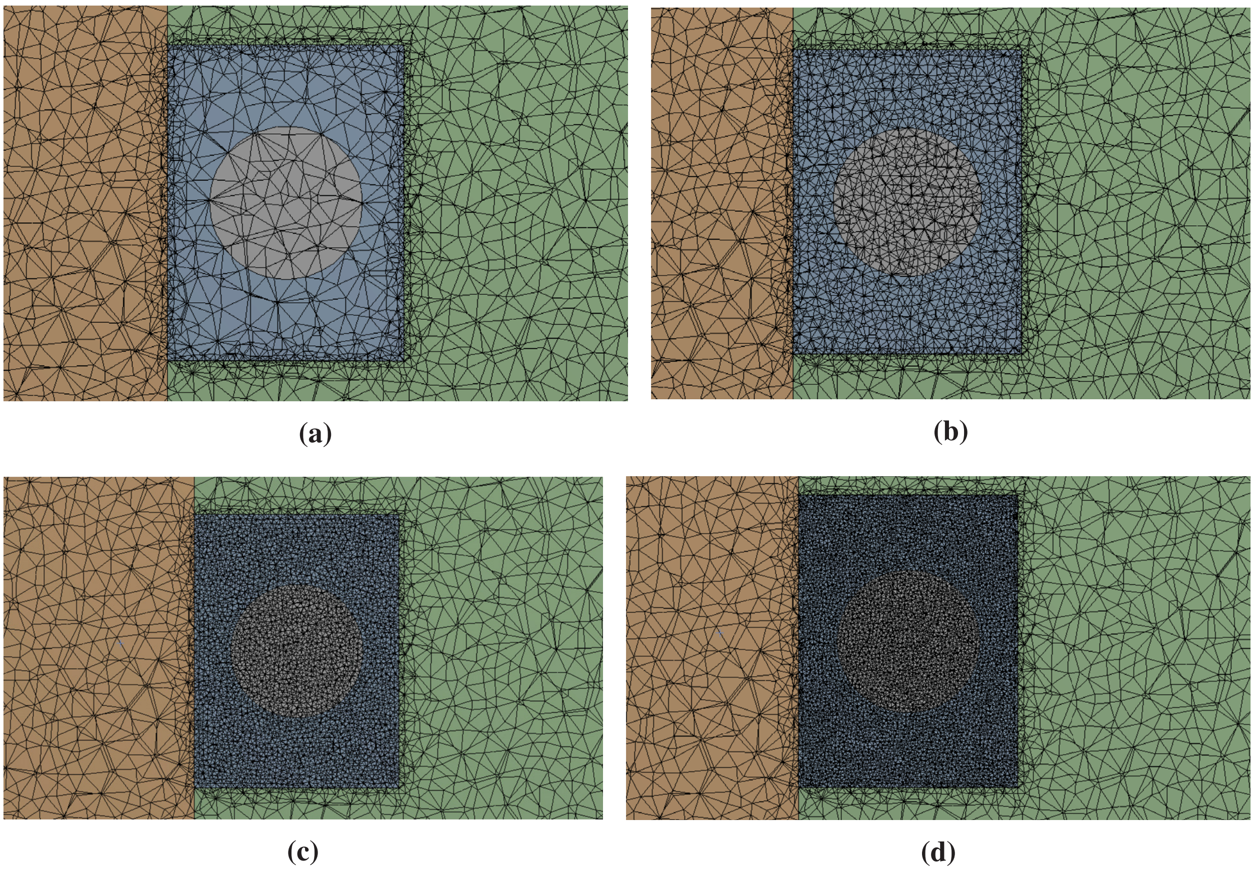

Fig. 8. Comparison of FEM volume discretization of four internal size steps, (a) 0.04, (b) 0.015, (c) 0.008 and (d) 0.006 m

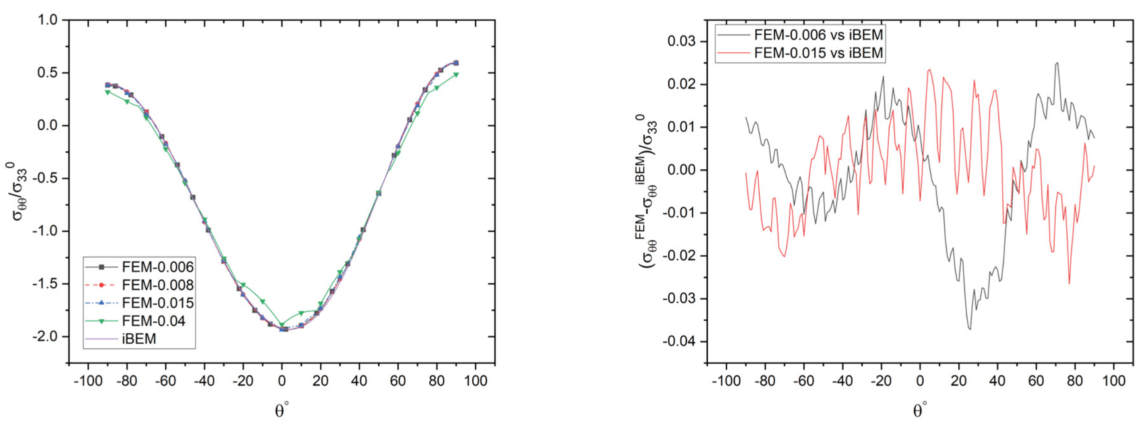

(a) **(b)**

Fig. 9. (a) Comparison of stress concentration factor $\sigma_{\theta\theta}/\sigma_{33}^{0}$ among iBEM and FEM with four internal size steps; (b) Error analysis of stress concentration factor $\sigma_{\theta\theta}/\sigma_{33}^{0}$ between iBEM and FEM with 0.015 and 0.006 size steps